Negative Index Photonic Crystals Superlattices and Zero Phase Delay Lines

C. W. Wong et al.,[*]

Columbia University, New York, NY
USA

1. Introduction

An intense interest in negative index metamaterials (NIMs) [1-2] has been witnessed over the last years. Metal based NIMs [3-11] have been demonstrated at both microwave and infrared frequencies with a motivation mainly coming from the unusual physical properties and potential use in many technological applications [12-21]; however, they usually have large optical losses in their metallic components. As an alternative, dielectric based photonic crystals (PhCs) have been shown to emulate the basic physical properties of NIMs [22-26] and, in addition, have relatively small absorption loss at optical frequencies. Equally important, PhCs can be nanofabricated using currently available silicon chip-scale foundry processing, allowing significant potential in the development of future electronic-photonic integrated circuits.

One particular type of PhC can be obtained by cascading alternating layers of NIMs and positive index materials (PIMs) [27 – 32]. This photonic structure (with an example shown in Figure 1) is postulated to show unusual and unique optical properties including new types of surface states and gap solitons [33], unusual transmission and emission properties [34 – 38], complete photonic bandgaps [39], and phase-invariant field that can be effectively used in cloaking applications [40]. Moreover, a remarkable property of these binary photonic structures is the existence of an omnidirectional bandgap that is insensitive to the wave polarization, angle of incidence, structure periodicity, and structural disorder [41 – 43]. The main reason for the occurrence of a bandgap with such unusual properties is the existence of a frequency band at which the path-averaged refractive index is equal to zero [27 – 32, 34]. Specifically, at this frequency the Bragg condition, $k\Lambda = (\bar{n}\,\omega/c)\Lambda = m\pi$, is satisfied for $m = 0$,

[*] S. Kocaman[1], M. S. Aras[1], P. Hsieh[1], J. F. McMillan[1], C. G. Biris[2], N. C. Panoiu[2], M. B. Yu[3], D. L. Kwong[3] and A. Stein[4]

[1]*Columbia University, New York, NY,*
[2]*University College of London, London,*
[3]*Institute of Microelectronics, Singapore,*
[4]*Brookhaven National Laboratory, Upton, NY,*
[1,4]*USA*
[2]*UK*
[3]*Singapore*

irrespective of the period Λ of the superlattice; here, k and ω are the wave vector and frequency, respectively, and $\bar{n}$ is the averaged refractive index. Because of this property this photonic bandgap is called zero-$\bar{n}$, or zero-order, bandgap [30, 34].
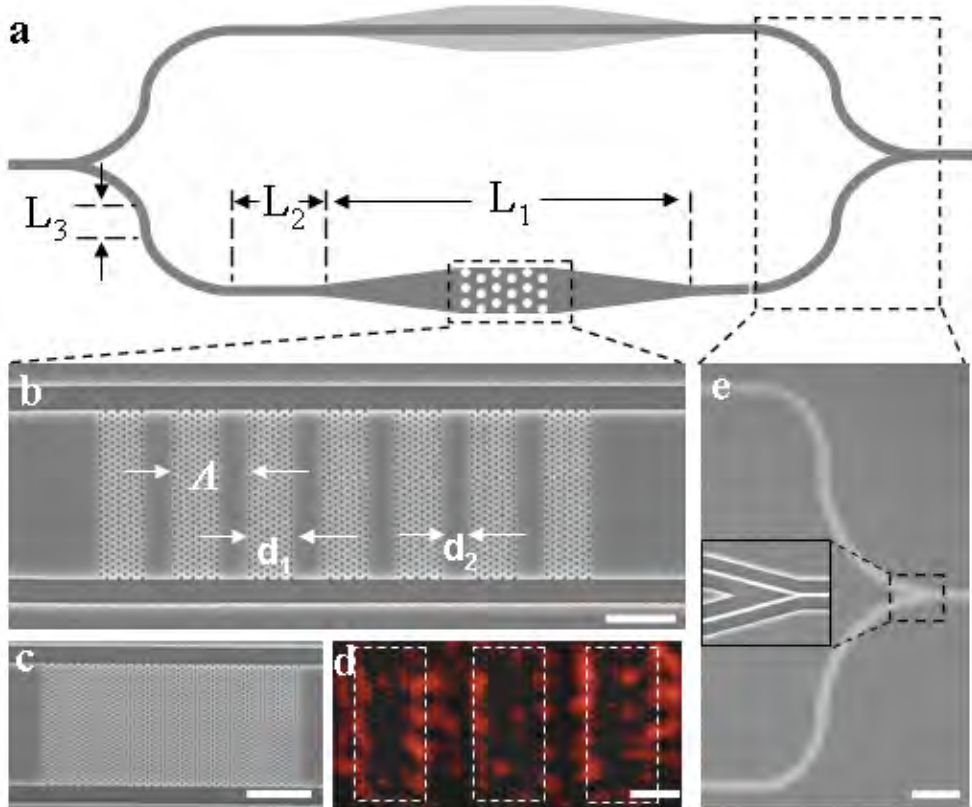

Fig. 1. **Schematic of a Mach-Zehnder interferometer (MZI) and SEM images of the fabricated device. a,** Schematic representation of the MZI. $L_1 \sim 850$ µm and $L_2 \sim 250$ µm. **b,** SEM of a fabricated superlattice with 7 super-periods. Each PhC layer contains 7 unit cells of PhC (d_1=2.564 µm, Λ=4.51 µm) with a=423 nm, r/a = 0.276, and t/a = 0.756 (the scale bar = 5 µm). **c,** SEM of a sample, showing only the PhC layer with same parameters as in **b** (the scale bar = 10 µm). **d,** Near-field image of a supperlattice with each PhC layer containing 9 unit cells (d_1=3.297 µm) (the scale bar = 2.5 µm). **e,** SEM of the Y-branch with a zoomed-in image in the inset (the scale bar = 25 µm).

Near-zero index materials have a series of exciting potential applications, such as diffraction-free beam propagation over thousands of wavelengths via beam self-collimation [34], extremely convergent lenses and control of spontaneous emission [35], strong field enhancement in thin-film layered structures [37], and cloaking devices [40]. Moreover, the vanishingly small value of the refractive index of near-zero index materials can be used to engineer the phase front of electromagnetic waves emitted by optical sources or antennas,

namely, to reshape curved wave fronts into planar ones [36], or to transfer into the far-field the phase information contained in the near-field. In addition, at the frequencies at which the refractive index becomes vanishingly small the electromagnetic field has an unusual dual character, i.e., it is static in the spatial domain (the phase difference between arbitrary spatial locations is equal to zero) while remaining dynamic in the time domain, thus allowing energy transport. This remarkable property, which is also the main topic of our study, has exciting technological applications to delay lines with zero phase difference, information processing devices, and the development of new optical phase control and measurement techniques.

In this chapter, we show unequivocally that optical beams propagating in path-averaged zero-index photonic crystal superlattices can simultaneously have zero phase delay. The nanofabricated superlattices consist of alternating stacks of negative index photonic crystals and positive index homogeneous dielectric media, where the phase differences corresponding to consecutive primary unit cells are measured with integrated Mach-Zehnder interferometers. These measurements demonstrate that at path-averaged zero-index frequencies the phase accumulation remains constant despite increases in the physical path lengths. We further demonstrate experimentally for the first time that these superlattice zero-$\bar{n}$ bandgaps can either remain invariant to geometrical changes of the photonic structure or have a center frequency which is deterministically tunable. The properties of the zero-$\bar{n}$ gap frequencies, optical phase, and the effective refractive indices agree well between the series of measurements and the complete theoretical analysis and simulations.

2. Negative refraction photonic crystal superlattices

2.1 Theory

The photonic structures examined consist of dielectric PhC superlattices with alternating layers of negative index PhC and positive index homogeneous slabs, as shown in Figure 1 and Figure 2, that can give rise to the zero-$\bar{n}$ gaps [29]. The hexagonal PhC region (Figure 1c) is made of air holes etched into a dielectric Si slab (n_{Si}=3.48), with a lattice period a = 423 nm, a slab thickness t = 320 nm, placed on top of a silica substrate (n_{SiO2}=1.5). The band diagram of the PhC with a hole-to-lattice constant (r/a) ratio of 0.276 ($r \sim$ 117 nm) is shown in Figure 3a-b. Particularly the two-dimensional (2D) hexagonal PhC base unit has a negative index within the interested spectral band of 0.271 to 0.278 in normalized frequency of $\omega a/2\pi c$, or 1520 to 1560 nm wavelengths, such as reported earlier for near-field imaging [22]. The zero-$\bar{n}$ superlattices are then integrated with Mach–Zehnder interferometers (MZI) to facilitate the phase delay measurements. As illustrated in Figure 1a, the unbalanced interferometer is designed such that after splitting from the Y-branch (Figure 1e); a single mode input channel waveguide adiabatically tapers (over $\sim$ 400 µm) to match the width of the superlattice structures. On the reference arm, there is either a slab with exactly the same geometry to match the index variations and hence isolate the additional phase contribution of the PhC structures, or a channel waveguide leading to a large index difference and hence to distinctive Fabry-Perot fringes. For the one-dimensional (1D) binary superlattice of Figure 1b, a near-field scanning optical microscope image is taken (Figure 1d) to confirm transmission near the zero-$\bar{n}$ gap edge (1560 nm). The period of the superlattice is equal to

$\Lambda = d_1 + d_2$ where $d_{1(2)}$ is the thickness of the PhC (PIM) layer in the primary unit cell. Since a zero-$\bar{n}$ bandgap is formed when the spatially averaged index is zero, it is insensitive to the variation of the superlattice period, as long as the condition of zero-average index is satisfied [27 – 31, 34].
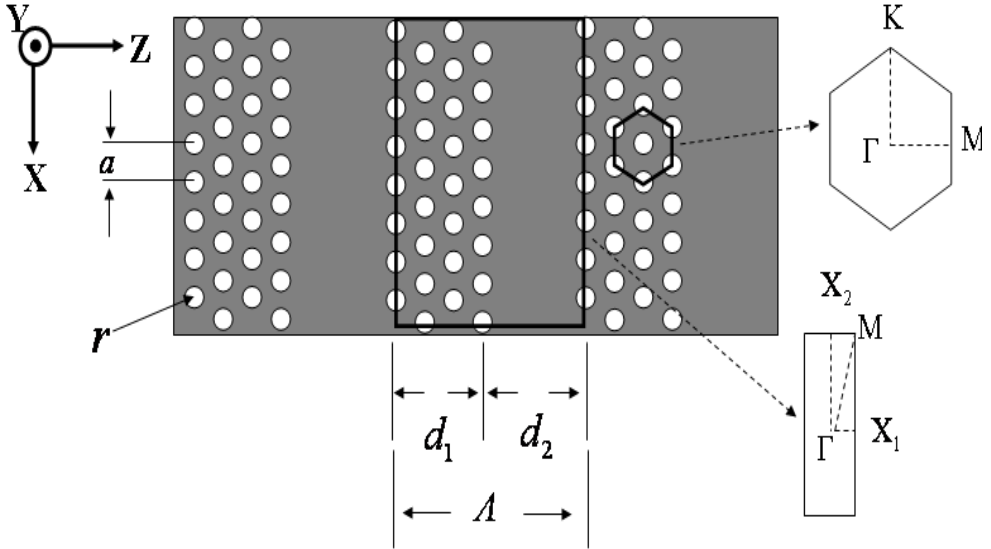

Fig. 2. **Schematic representation of the photonic superlattice.** There are two Brillouin zones defined as follows: one for the hexagonal photonic crystal lattice and one for the photonic superlattice. *a* is the lattice period and *r* is the radius of the holes forming the hexagonal lattice. d_1 is the length of the PhC layer and d_2 is the length of the PIM region. $d_1 + d_1 = \Lambda$ is equal to the superperiod (SP) of the photonic superlattice.

The existence of the zero-$\bar{n}$ bandgaps can be explained with the Bloch theorem, where for a 1D binary periodic lattice the trace of the transfer matrix, T, of a primary unit cell can be expressed as [27,29]

$$\text{Tr}\left[T(\omega)\right] = 2\cos(\kappa\Lambda) = 2\cos\left(\frac{\bar{n}\omega\Lambda}{c}\right) - \left(\frac{Z_1}{Z_2} + \frac{Z_2}{Z_1} - 2\right)\sin\left(\frac{n_1\omega d_1}{c}\right)\sin\left(\frac{n_2\omega d_2}{c}\right) \qquad (1)$$

where $n_{1(2)}$ and $Z_{1(2)}$ are the refractive index and impedance of the first (second) layer, respectively, κ is the Bloch wave vector of the electromagnetic mode, $\bar{n}$ is the average refractive index, $\bar{n}(x) = \frac{1}{\Lambda}\int_0^\Lambda n(x)dx$. In the general case, when $Z_2 \neq Z_1$, if $\kappa_0\Lambda = \frac{\bar{n}\omega\Lambda}{c} = m\pi$, with m an integer, the relation

$$\left|\text{Tr}\left[T(\omega)\right]\right| = \left|2 + \left(\frac{Z_1}{Z_2} + \frac{Z_2}{Z_1} - 2\right)\sin^2\left(\frac{n_1\omega d_1}{c}\right)\right| \geq 2 \qquad (2)$$

holds. This relation implies that the dispersion relation has no real solution for κ unless $\dfrac{n_1 \omega d_1}{c}$ is an integer multiple of π, which is the Bragg condition and thus photonic bandgaps are formed at the corresponding frequencies. However, if the lattice satisfies the special condition of a spatially averaged zero refractive index ($\bar{n} = 0$), again $\left| \text{Tr} \left[T(\omega) \right] \right| \geq 2$, thereby leading to imaginary solutions for the wave vector κ and thus to a spectral gap [30 – 32]. We also note that the 1D binary superlattice and the hexagonal PhC have different symmetry properties and therefore different first Brillouin zones (see Figure 2a-insets). Schematic representation of a superlattice with 3 superperiods is shown in Figure 2. The superlattice consists of alternating layers of hexagonal PhCs and homogeneous slabs.

In our fabricated devices, the longitudinal direction of the superlattice (z-axis) coincides with the Γ-M axis of the hexagonal PhC. Moreover, within our operating wavelength range (Figure 3b) the PhC has two TM-like bands, one with positive index and the other one with negative index, and an almost complete TE-like bandgap (see Methods). The effective refractive indices corresponding TM-like bands (Figure3b) are determined from the relation $k = \omega |n|/c$ and plotted in Figure 3c (note that for the second band the effective index of refraction is negative since k decreases with ω [22]).

2.2 Mach-Zehnder interferometer with negative index photonic crystal

To examine effective index differences between different bands in the band diagram experimentally, we designed and fabricated 100 unit cells of PhC and a geometrically identical homogeneous slab on the two arms of the MZI. Example scanning electron micrographs (SEMs) are shown in Figure 1. Transmission is measured with amplified spontaneous emission source, in-line fiber polarizer with a polarization controller to couple the light in with a tapered lensed fiber, and an optical spectrum analyzer. In the transmission (Figure 3d; black), the MZ interference spectra has two steep variations, first at the end of the first band (negative index band) and second at the start of the second band (positive index band). This is a clear indication of an abrupt refractive index change (Figure 3c) that is only possible when there is an abrupt interband transition between two bands. The non-MZI transmission spectrum of a similar structure is also shown in Figure3d (red) for reference.

To characterize this steep index change further we placed on the two arms of the MZI PhC sections with different radius r. We kept a unchanged in order to have the same total physical length on both arms, for the same number of unit cells in the PhC sections. With this approach, the MZI sections that do not contain PhC regions are identical and hence one isolates the two PhC sections as the only source for the measured phase difference. For instance, we set r_2 to 5/6 of the original value of the radius r_1 ($r_2/a = 0.283 \times 5/6 = 0.236$). Figure 4a illustrates the difference between the band structures of the two PhC designs, namely, a frequency shift of the photonic bands. Due to this shifted band structure, the accumulated phase difference between the two arms is almost independent of wavelength, except for a steep variation that again corresponds to a steep refractive index change (moving from band to band). When we place a section of 62 PhC unit cells in both arms of the MZI, the transmission spectra presents two spectral domains, 1525 nm to 1550 nm and

1580 nm to 1615 nm, where the interference transmission is rather constant (red curve in Figure 4b) with ~ 14dB transmission difference between the two domains. In the next section, we show high spatial resolution images for this experiment.
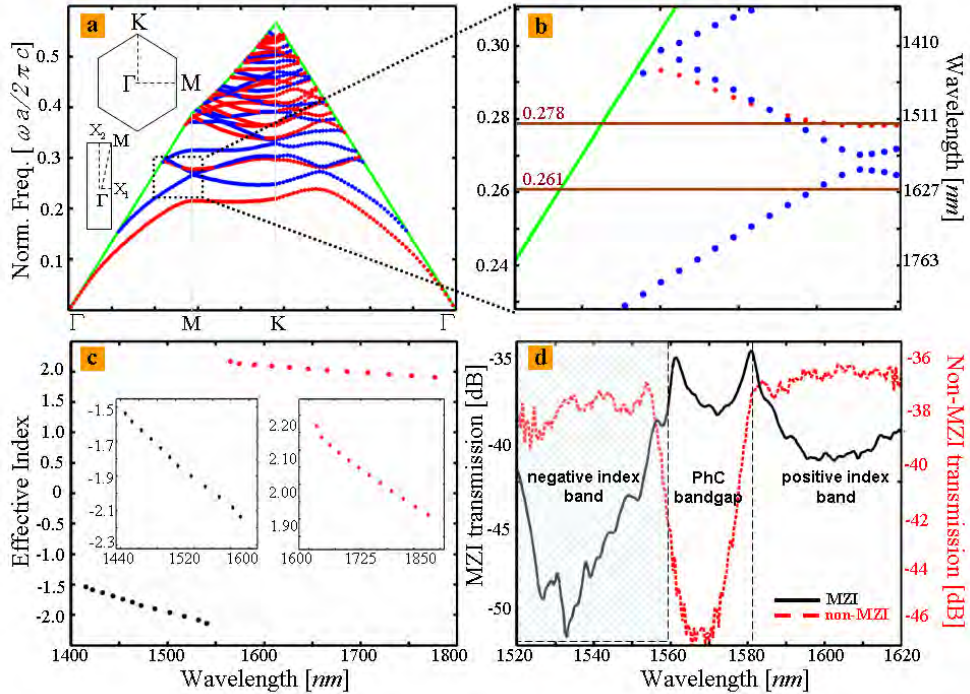

Fig. 3. **Band diagram of the PhC and the calculated effective index. a,** Band diagram of the PhC with the parameters given in Figure1. Insets: first Brillouin zones of the hexagonal PhC (top) and the 1D superlattice (bottom). The TM-like (TE-like) photonic bands are depicted in blue (darker) [red (lighter)]. The light cone is denoted by the green lines. **b,** A zoom-in of the spectral domain corresponding to experimental region of interest. Experiments were performed in the spectral region marked by the two horizontal lines. **c,** Calculated effective index of refraction of the PhC, corresponding to the two TM-like bands shown in Figure2b. Insets: zoom-in of the two bands. **d,** Black (solid) line: MZI transmission with 100 unit cells of PhC on one arm and an homogeneous slab waveguide on the other arm. Red (dashed) line: transmission spectrum for non-MZI PhC superlattice with 60 unit cells.
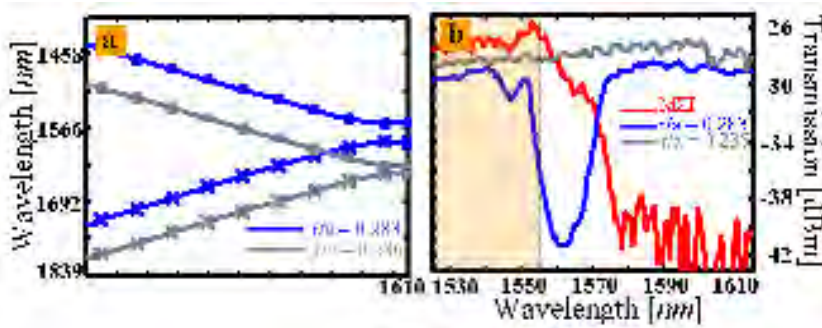
Fig. 4. **Mach-Zehnder interferences with negative refraction PhCs. a,** Band diagram shifts to lower frequency when the *r/a* ratio changes. Blue is the original design and gray is the design with *r/a*=0.236. **c.** Red line: MZI transmission with 62 unit cells of PhC on one arm with *r/a*=0.283 and 62 unit cells of PhC with *r/a*=0.236 on the other arm; the lattice period (*a*) is the same in both cases. Blue (grey) line: Transmission spectrum for PhC superlattice with *r/a*=0.283 (0.236) and 80 unit cells of PhC. Different index differences (*Δn*) from 1525 nm to 1550 nm and from 1580 nm to 1615 nm give different phase difference (*ϕ*) and different interference output.

2.3 Spatial field distribution

In addition, we performed high spatial resolution imaging of the radiated input-output ports for the devices that have been used for the experiment presented in Figure 4. Results are illustrated in the Figure 5 as follows: In the case of the reference arm (**i-iii**), we see light transmission for all three wavelengths, which corroborates the characteristics of the transmission spectrum in Figure 4b. For the device arm (**iv-vi**) there is transmission for 1600 nm and 1530 nm but not for 1570 nm. This agrees with the transmission spectra in Figure 4b. Note that although there is similar transmission for both arms at 1530 and 1600 nm, the interference output has 14dB difference.

3. Existence of zero-n gap

The band diagram in Figure 3a is calculated by using *RSoft's BandSOLVE* [45], a commercially available software that implements a numerical method based on the plane wave expansion of the electromagnetic field. 3D simulations have been performed to calculate 30 bands and for each band the corresponding values of the effective refractive index have also been determined. In all these numerical simulations a convergence tolerance of 10^{-8} has been used. The photonic bands have been divided into TM-like and TE-like, according to their parity symmetry. The path-averaged index of the superlattice has been calculated by using the negative effective index of the second TM-like band and the effective modal index of the homogeneous asymmetric slab waveguide.

3.1 Numerical simulations

In order to investigate numerically the spectral properties of the transmission characterizing a specific photonic superlattice, we have employed three-dimensional (3D) simulations

based on the finite-difference time-domain (FDTD) algorithm; for this, we have used Rsoft's FullWAVE [45]. In our calculations we have studied three superlattices, each with a different period Λ: they have 7, 11 and 15 unit cells along the z-axis, in the PhC layer, so that the thickness of this layer is $d_1 = 3.5\sqrt{3}\,a$, $d_1 = 5.5\sqrt{3}\,a$, and $d_1 = 7.5\sqrt{3}\,a$, respectively. The corresponding thickness of the PIM layer has been calculated by requiring that the average of the index of refraction is zero that is $\bar{n} = (n_1 d_1 + n_2 d_2)/\Lambda = 0$ [28], while keeping the ratio d_2/d_1 unchanged. Importantly, n_1 and n_2 are the *effective indices* of the modes in the PhC and homogeneous layers, respectively, at the corresponding wavelength. We performed this numerical analysis for superlattices with ratio d_2/d_1=0.746 (design 1) and d_2/d_1=0.794 (design 2). Thus by changing the ratio d_2/d_1 we can investigate the dependence of the wavelength at which the zero-$\bar{n}$ gap is observed on the period of the superlattice. We expect to see the zero order gap in the design 2 at a different frequency, as compared to the frequency of the zero order gap in the design 1, a frequency at which the effective indices again satisfy the equation $\bar{n} = (n_1 d_1 + n_2 d_2)/\Lambda = 0$. The effective index of the PIM layer, n_2, can be calculated analytically, as it corresponds to the TM modes of an asymmetric slab waveguide; at λ=1550 nm it is n_2=2.648. Similarly, the effective index corresponding to the second TM-like band shown in Figure 1d is determined from the relation $k=\omega|n|/c$ (note
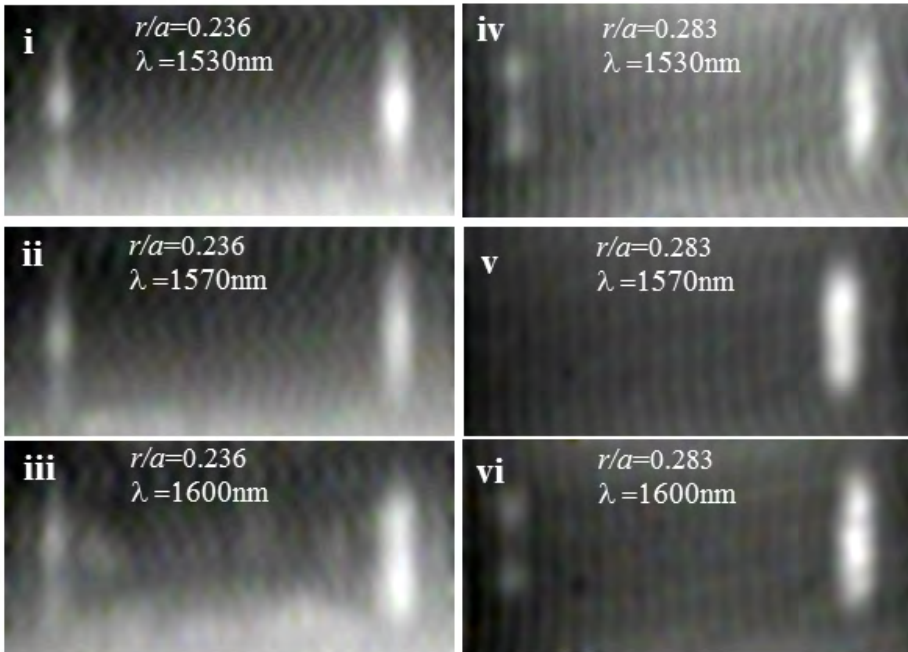

Fig. 5. **Infrared images pertaining to the experiments corresponding to Fig3c. i-iii** is taken from the reference arm containing a PhC structure with *r/a*=0.236 and **iv-vi** is taken from the device arm where the ratio *r/a*=0.283. In all the images the input beam is impinging onto the structure from the right, which means that light scattering at the left facet of the device indicates light transmission.

that for the second band the effective index is negative since ω decreases with k [31]). At normalized frequencies of $\omega a/2\pi = 0.295$ and $\omega a/2\pi = 0.276$, the effective index of refraction is approximately –1.604 and –1.988, respectively.

In Figure 6a, the results of the 3D FDTD simulations are summarized, for all three superlattices (7, 11, and 15 unit cells), each have a ratio $d_2/d_1 = 0.746$. In order to observe clear gaps, 5 stacks were used in the case of 7 unit cells in the PhC layer, whereas in the cases with 11 and 15 unit cells in the PhC layer 3 stacks sufficed. The results of similar calculations, for $d_2/d_1 = 0.794$ are shown in Figure 6b. The grid size resolution in all our numerical simulations is $0.0833a$ (35 nm). Furthermore, we highlight the region where the PhC has negative index of refraction, which is the region of interest in our study. As illustrated in Figure 6a and Figure 3.6b, the transmission spectra show several gaps; however, except for an invariant gap located at $\omega a/2\pi = 0.276$ (Figure 6a; design 1) and $\omega a/2\pi = 0.272$ (Figure 6b; design 2), the mid-gap locations of the gaps change with the period of the superlattice. The shift in the mid-gap frequency with respect to the period is typical for regular Bragg gaps; the presence of an invariant gap, however, demonstrates the existence of zero-$\bar{n}$ gaps.
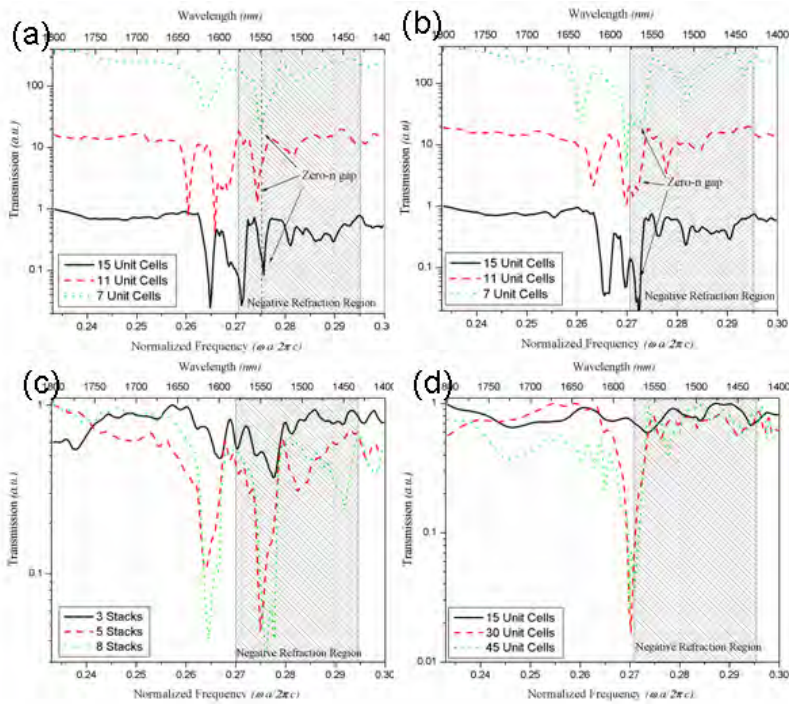

Fig. 6. (a) Transmission for a superlattice with $d_2/d_1 = 0.746$, containing 7, 11 and 15 unit cells in each PhC slab. 3 stacks in the PhC superlattice are used in the case when the PhC layers contain 11 and 15 unit cells, and 5 stacks for the case of PhC layers with 7 unit cells. (b) The same as in a), but $d_2/d_1 = 0.794$. (c) Transmission for a superlattice with $d_2/d_1 = 0.794$, containing 3, 5 and 8 stacks. Each PhC layer contains 7 unit cells. (d) Transmission trough a PhC slab containing 15, 30 and 45 unit cells. All results are obtained through full 3D FDTD numerical simulations.

To further investigate the nature of these photonic gaps, we next calculate the order, m, for the Bragg condition. The average index $\bar{n}$ and the value of $k_o\Lambda/\pi$ for the two deigns are summarized in Table 1. The average indices are -0.007 and 0.001 whereas the corresponding $k_o\Lambda/\pi$ values are 0.044 and 0.007 for design 1 and design 2, respectively. It is thus clear that these normalized gap frequencies ($\omega n/2\pi c$ = 0.276 for design 1 and $\omega n/2\pi c$ = 0.272 for design 2) correspond to zero-order gaps. Moreover, for both superlattices, in the frequency range of negative index of refraction there are other spectral gaps. For example, the gap at $\omega n/2\pi c$ = 0.283, corresponds to an average index of refraction of 0.091 (design 1) and 0.153 (design 2), with the corresponding $k_o\Lambda/\pi$ being 0.874 and 0.962, and thus it is a first-order gap. None of these gaps is due solely to the presence of the PhC layers, as the PhC band gap for the TM polarization is at $\omega n/2\pi c$ = 0.27 (see Figure3b).

Figure	Unit Cells of PhC	Gap Frequency	d_2/d_1	Effective Index		Average index, $\bar{n}$	$k_o\Lambda/\pi$	Gap order
				PhC	Slab			
Fig. 3.3a (design 1)	7	0.276	0.746	-1.988	2.648	-0.007	-0.044	0
Fig. 3.3a (design 1)	11	0.283	0.746	-1.844	2.684	0.091	0.874	1
Fig. 3.3b (design 2)	7	0.272	0.794	-2.080	2.622	0.001	0.007	0
Fig. 3.3b (design 2)	7	0.283	0.794	-1.856	2.683	0.153	0.962	1

Table 1. **Average refractive index of the corresponding gaps and the gaps' order**

As an additional proof that the invariant gap is not a band gap of the PhC, we present in Figure 6d the calculated transmission spectra of a PhC layer with a number of 15, 30, and 45 unit cells (no layers of homogeneous material is present in this case). Thus, this figure shows that the PhC gap is shifted by almost 40 nm from the location of the zero-order gap in gap Figure 6a. We also examined the dependence of the gap locations on the number of stacks in the superlattice. The results of these calculations are presented in Figure 6c for stack numbers 3, 5, and 8. We observe that the zero-$\bar{n}$ gap location has not changed and, as expected, it becomes deeper as the number of stacks increases.

3.2 Electric field distribution

We have also calculated the electric field distribution in the zero-n superlattice for different wavelengths in our experimental region in continuous wave excitation type. In order to be able to get this distribution, we have run the simulation until it gets to steady state and then save the field. Next, we launched another simulation with an input field by using this saved field and ran for only one cycle by saving electric field in small steps. Then we have averaged the $|E|^2$ and plotted. Figure 7 shows the results.
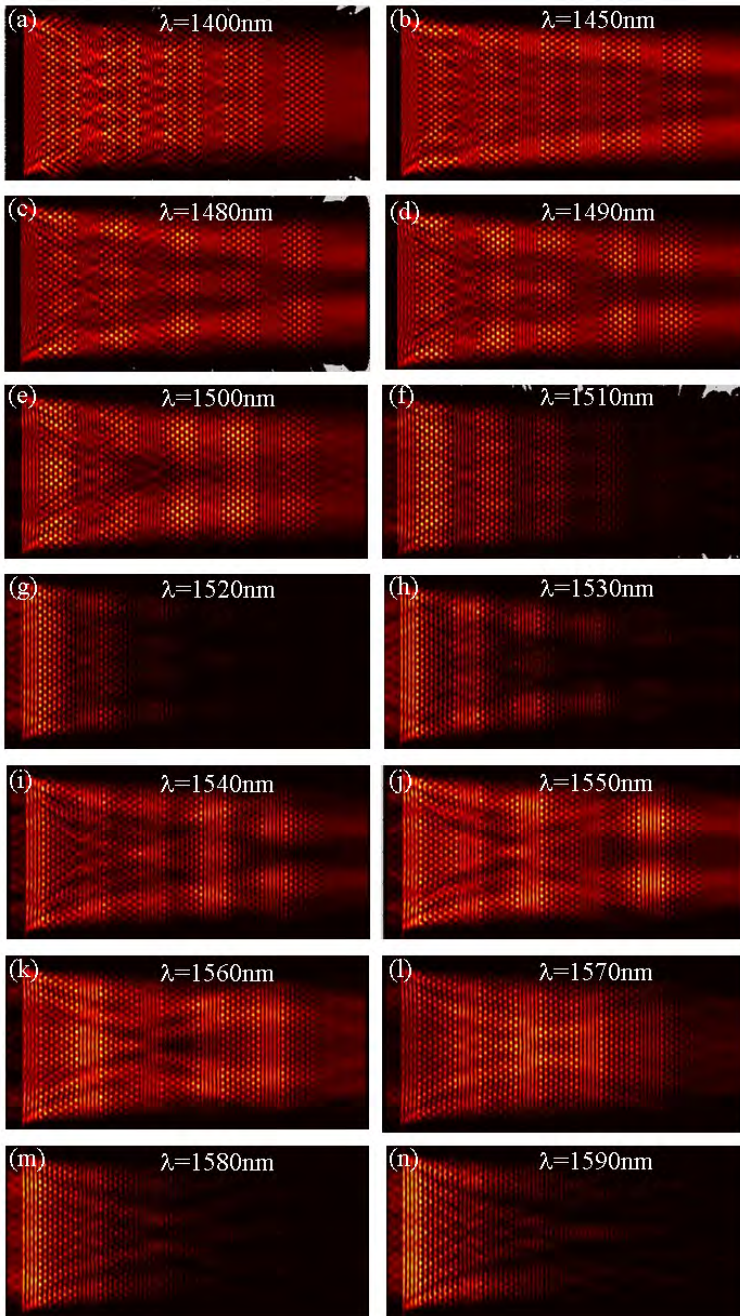
Fig. 7. A time-averaged steady-state distribution of the field intensity, $|E|^2$, corresponding to a propagating mode with different wavelengths within the experimental region.

3.3 Device nanofabrication and experiments

Our theoretical predictions are validated by a series of experiments. Thus, we have fabricated in a single-crystal silicon-on-insulator substrate samples with 3, 5 and 8 stacks whose PhC layers have thickness of $d_1 = 3.5\sqrt{3}\ a$. The silicon device height is 320 nm and the silicon oxide cladding thickness is 1 μm. The PhC superlattice is lithographically patterned with a 248-nm lithography scanner, and the Si is plasma-etched. Figure 1b shows an example of a fabricated photonic crystal superlattice with 8 stacks. The fabrication disorder in the PhC slab was statistically parameterized [37], with resulting hole radius 122.207 ± 1.207 nm, lattice period 421.78 ± 1.26 nm (~ 0:003a), and ellipticity 1.21 nm ± 0.56 nm. These small variations are below ~0:05a disorder theoretical target [46].

Incident light from tunable lasers between 1480 nm to 1690 nm (0.248 to 0.284 in normalized frequency of $\omega a/2\pi$) is coupled into the chip *via* tapered lensed fibers with manual fiber polarization control. The transmission for the TM polarization is measured, with each transmission measurement averaged over three scans. Figure 8a shows the transmission spectrum for design 1 (with d_2/d_1 = 0.746); it shows two distinct spectral dips, centered at 1520 nm ($\omega a/2\pi \approx 0.276$) and 1585 nm ($\omega a/2\pi \approx 0.265$). We then repeat these transmission measurements for a second design (design 2; d_2/d_1 = 0.794); the corresponding results are shown in Figure 8b. Similar to the spectra in Figure 8a, this figure shows a distinct spectral dip, located near the normalized frequency $\omega a/2\pi \approx 0.272$, *i.e.* at λ=1543 nm. Furthermore, the frequency spectral dip at $\omega a/2\pi \approx 0.262$ is weaker than in design 1, which is due to the fact that below a certain frequency, $\omega a/2\pi \approx 0.265$, the detected power is not high enough for observing the spectral features.

Figure 8c shows the near-infrared image captured with incident laser at 1550 nm and corresponds to the design 1. The spatially alternating vertical stripes show radiation scattered at the interfaces between the PhC and the homogeneous layers and confirm the transmission of the light through the superlattice. The near-infrared images also confirm the existence of the dip in the transmission spectrum, with most of the light being reflected and only a small amount propagating out of the output facet of the third stack (in this figure , the incident laser is tuned to the zero-n̄ gap frequency).

To better understand the results of these measurements, we repeated the FDTD simulations for the case of the fabricated devices. A good match between the results of the measurements and those of simulations, in terms of *absolute* values of the frequencies, has been observed for both values of the ratio d_2/d_1 (design 1 and 2) and varying stack numbers (design 1). The theoretical predictions are shown as the dotted lines in Figure 8a and 3.8b.

Figure 8d further shows the results of a series of experiments for PhC superlattices of design 1, each with 7 unit cells but with increasing number of stacks, from 3 to 5 and 8. As observed, both gaps become deeper with increasing number of stacks. It should be noted that by improving the impedance matching between the negative and positive index materials, transmission spectrum for even larger number of stacks in the PhC superlattice can be observed. The center-frequency of the gaps does not change when the number of stacks increases, the slight deviations in the gap frequency being attributable to small variations in the dimensions of the fabricated superlattice structures. This series of measurements further reinforce the observation of the zero-n̄ gap in cascaded negative- and positive-refraction superlattices.
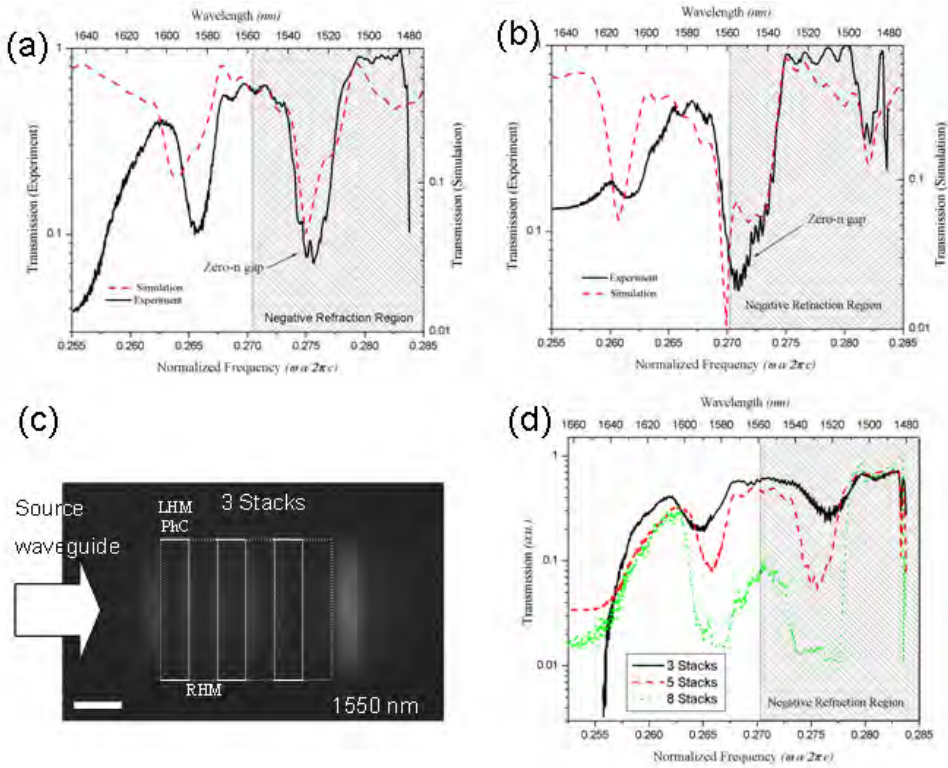
Fig. 8. (a) Measured transmission for a superlattice with d_2/d_1= 0.746, with 7 unit cells in the PhC layers and 5 stacks; for comparison, results of numerical simulations are also shown. (b) The same as in a), but for a superlattice with 0.794. (c) Example of near-infrared top-view image of a device with 3 stacks, from transmission measurement at 1550 nm. Superimposed are the locations of the negative refraction PhC and positive index material in the superlattice. Scale bar: 2 µm. (d) Measured transmission for a superlattice with d_2/d_1= 0.746, with 3, 5 and 8 stacks and 7 unit cells in the PhC layers. Both gaps become deeper as the number of stacks increases.

It has been pointed out that zero-$\bar{n}$ gaps can be omnidirectional [28, 41]; however, in our case, due to the anisotropy of the index of refraction of the PhC, the zero-$\bar{n}$ gap is not omnidirectional. Moreover, varying the lattice period, radius, and the thickness of the superlattice, and thus changing the frequency at which the average effective index of refraction is equal to zero, the frequency of the zero-$\bar{n}$ gap can be easily tuned as we show in the next section. Importantly, we note the demonstration of these zero-$\bar{n}$ gap structures can have potential applications as delay lines with zero phase differences which we also show later in this chapter.

4. Tunability of zero-n gap

Next, in order to demonstrate the tunable character of the zero-$\overline{n}$ bandgaps, we performed transmission experiments on four sets of binary superlattices, with each set having different superlattice ratios: d_2/d_1=0.74 (Figure 9a), d_2/d_1=0.76 (Figure 9b), d_2/d_1=0.78 (Figure 9d), and d_2/d_1=0.8 (Figure 9e). In all our experiments the negative index PhC has the same parameters as those given above. Each set has three devices of different periods Λ, with the negative index PhC layer in the superlattice spanning 7, 9, and 11 unit cells along the z-axis similar to the numerical study in 3.1, so that the thickness of this layer is $d_1 = 3.5\sqrt{3}$ a (2.564 μm), $d_1 = 4.5\sqrt{3}$ a (3.297 μm), and $d_1 = 5.5\sqrt{3}$ a (4.029 μm), respectively. The corresponding thickness of the PIM layer is determined by requiring that the average index is zero [$\overline{n} = (n_1 d_1 + n_2 d_2)/\Lambda = 0$], while keeping the ratio d_2/d_1 unchanged for all devices in each set (see Table 2). Here, n_1 and n_2 are the effective mode indices in the PhC and homogeneous layers respectively at the corresponding wavelengths. For the three devices in each set, we designed 7 super-periods (SPs) for the devices with 7 unit cells of PhC and 5 SPs for those with 9 and 11 unit cells of PhC (these designs ensure a sufficient signal-to-noise ratio for the transmission measurements). In these experiments we have tested both the existence of the zero-$\overline{n}$ bandgap as well as its tunability. For the three devices belonging to each set, we observed the zero-$\overline{n}$ bandgap at the same frequency whereas the spectral locations of the other bandgaps were observed to shift with the frequency – this confirms the zero-$\overline{n}$ bandgap does not depend on the total superperiod length Λ (gap existence dependent only

Figure 9a			
# of unit cells	d_1	d_2	Λ
7	2.56	1.90	4.46
9	3.30	2.44	5.74
11	4.03	2.98	7.01
Figure 9b			
# of unit cells	d_1	d_2	Λ
7	2.56	1.95	4.51
9	3.30	2.51	5.80
11	4.03	3.06	7.09
Figure 9d			
# of unit cells	d_1	d_2	Λ
7	2.56	2.00	4.56
9	3.30	2.57	5.87
11	4.03	3.14	7.17
Figure 9e			
# of unit cells	d_1	d_2	Λ
7	2.56	2.05	4.62
9	3.30	2.64	5.93
11	4.03	3.22	7.25

Table 2. **Calculated parameters of the devices in the Figure 9 (units in μm).**

on the condition of path-averaged zero index: $n_1 d_1 + n_2 d_2 = 0$) while the frequency of the regular 1D PhC Bragg bandgaps does depend on Λ. Our measurements show that the invariant, zero-$\bar{n}$, bandgap is located at 1525.5 nm, 1535.2 nm, 1546.3 nm, and 1556.5 nm, respectively (averaged over the three devices in each set). The slight red-shift with increasing number of unit cells in each set is due to effects of edge termination between the PhC and the homogeneous slab.
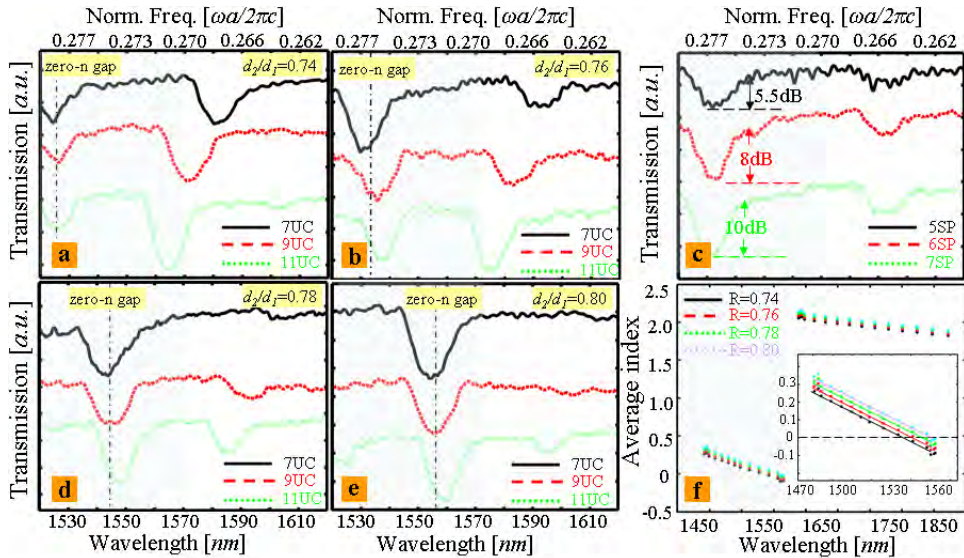

Fig. 9. **Experimental verification of period-invariance and tunability of zero-$\bar{n}$ bandgaps.**
a, Experimental verification of the zero-$\bar{n}$ bandgap in superlattices with varying period (Λ). The ratio d_2/d_1 =0.74 and Λ=4.46 µm for black (solid), 5.74 µm for red (dashed), and 7.01 µm for green (dotted) curves (*a.u.* arbitrary units). The lightly shaded regions in all panels denote the negative index regions. **b,** Same as in **a,** but for d_2/d_1 =0.76. Λ=4.51 µm for black (solid), 5.80 µm for red (dashed), and 7.09 µm for green (dotted) curves. **c,** Transmission spectra for superlattices with d_2/d_1 =0.76, containing 5, 6, and 7 unit cells (UC). Each PhC layer contains 7 unit cells (d_1=2.564 µm , Λ=4.51µm). **d,** Same as in **a,** but for d_2/d_1 =0.78. Λ=4.56 µm for black (solid), 5.87µm for red (dashed), and 7.17 µm for green (dotted) curves. **e,** Same as in **a,** but for d_2/d_1 =0.80. Λ=4.61 µm for black (solid), 5.93 µm for red (dashed), and 7.25 µm for green (dotted) curves. **f,** Calculated effective index of refraction for the superlattices with the ratios in **a, b, d,** and **e.** The wavelengths at which the average index of refraction cancels agree very well with the measured values.

Furthermore, when we tuned the ratio d_2/d_1 and repeated these same experiments we observed a redshift of the zero-$\bar{n}$ mid-gap frequency as we increased the ratio d_2/d_1. This result is explained by the fact that for the negative index band the refractive index of the 2D hexagonal PhC decreases with respect to the wavelength (see Figure 3c) and therefore when the length of the PIM layer in the 1D binary superlattice increases (higher d_2/d_1), the wavelength at which the effective index cancels is red-shifted. The effective index of the PIM

layer, n_2, is calculated numerically and for the asymmetric TM slab waveguide mode corresponds to, for example, 2.648 at 1550 nm. By using these n_1 (Figure 3c) and n_2 values, we determined the average refractive index for the different d_2/d_1 ratios as summarized in Figure 9f. A distinctive red-shift in the zero-$\bar{n}$ gap location is observed with increasing d_2/d_1 ratios from the numerically modeling, demonstrating good agreement with the experimental measurements (Figure 9a, 9b, 9d, and 9e) without any parameter fitting in the analysis. Furthermore, Figure 9c shows how the spectral features of the zero-$\bar{n}$ bandgap changes with increasing the number of superperiods and the results are similar to those in Figure8d as expected. We note that this is the first rigorous and complete experimental confirmation of invariant and tunable character of zero-$\bar{n}$ bandgaps in photonic superlattices containing negative index PhCs.

5. Zero phase delay lines

Next, we prove that the total phase accumulation in the superlattice is zero. For this, we performed phase measurements for the designs with three different sets of measurements: **(a)** d_2/d_1=0.78 and 7 unit cells in the PhC layer; **(b)** d_2/d_1= 0.8 and 7 unit cells in the PhC layer; and **(c)** d_2/d_1= 0.8 and 9 unit cells in the PhC layer. In these series of measurements we used a single mode channel waveguide for the reference arm of the MZI – this enables a series of interference fringes at the output, which can be used to determine the phase change by analyzing the spectral location of the fringes and their free spectral range (FSR). In most free-space interferometric applications, the phase difference leading to interference originates from the physical length difference between the two arms, but in integrated photonic circuits this delay can easily be modulated by the imbalance in the refractive indices of two arms [47]. For **(a)** and **(c)**, we examined three devices, namely, superlattices with 5, 6, and 7 SPs and for **(b)** we tested superlattices with 5 and 7 SPs. When we designed these devices, we modified the MZI such that when we added a SP to the superlattice the length of the adiabatic transition arms was carefully increased by $\Lambda/2$, making the horizontal single mode channel waveguides shorter (from L_2 to L_2-$\Lambda/2$, at both sides in Figure 1a). This change is compensated by adding the same length to the vertical part (from L_3 to L_3+$\Lambda/2$ on both sides in Figure 1a). As a result, the only phase difference between devices is due to the additional SPs. This procedure is explained in Section 5.1 in detail.

5.1 Device modification for phase measurements

Figure 10 shows a schematic representation of a device with 2 superperiods and the integrated Mach Zehnder Interferometer is modified after introducing the third superperiod. The adiabatic region remains unchanged if L_1 is increased to L_1+Λ and L_2 is shortened by $\Lambda/2$, in both the input and output sides of the device. To keep the total length of the waveguide unchanged, the length L_3 is increased to L_3+ $\Lambda/2$. This procedure is used each time a superperiod is added to the structure. In addition, to be able to compare devices with different number of unit cells in the PhC layer, a common reference point is used for all devices that have the same d_2/d_1 ratio.

In our implementation, the interferometer output intensity is given as:

$$I = I_1 + I_2 + 2\sqrt{I_1 I_2} \cos\phi \tag{3}$$

where ϕ is the phase difference (or imbalance) between the modes propagating in the two arms (denoted by subscript 1 and 2). Considering our implementation, the phase ϕ can be decomposed as:

$$\phi = \phi_1 - \phi_2 = \frac{2\pi}{\lambda}\left[\left(n_{wg}L_{wg\_1} + n_{slab\_1}L_{slab\_1} + n_{sl}L_{sl}\right) - n_{wg}L_{wg\_2}\right]$$

$$= \frac{2\pi}{\lambda}\left[n_{wg}\left(L_{wg\_1} - L_{wg\_2}\right) + n_{slab\_1}L_{slab\_1}\right] + \frac{2\pi}{\lambda}n_{sl}L_{sl}$$

(4)

where n_{wg}, n_{slab_1}, n_{sl} are the effective mode refractive indices of the channel waveguide, the adiabatic slab in arm 1, and the zero-index superlattice, respectively. L_i denotes the corresponding lengths.
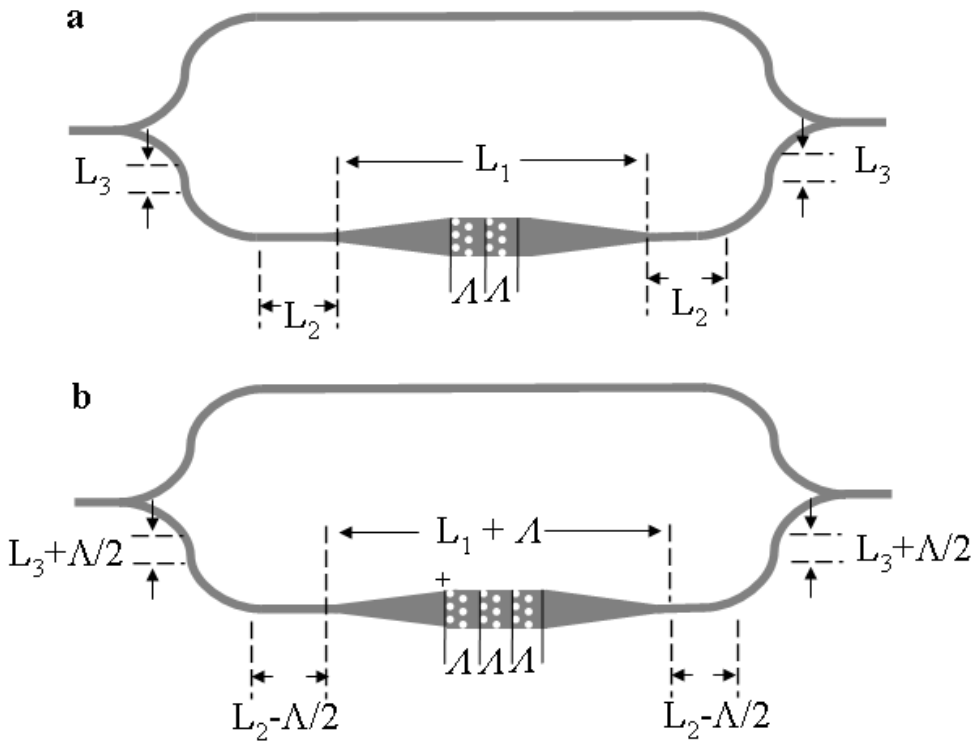

Fig. 10. **Schematic representation of the device modification induced by adding a superperiod. a,** Integrated MZI of a device with 2 superperiods and a channel waveguide. **b,** Device modifications after the third superperiod is added. The length of the channel waveguide remains the same so as the effect of the additional superperiod is isolated.

We note that the difference between the physical path length of the channel waveguides on both arms is designed to be equal to the physical path length of the tapering slab. Thus we have:

$$\cos[\phi] = \cos\left[\frac{2\pi}{\lambda}\left(\left(-n_{wg}L_{Slab\_1} + n_{Slab\_1}L_{Slab\_1}\right) + n_{sl}L_{sl}\right)\right]$$

$$= \cos\left[\frac{2\pi}{\lambda}\left(\left(n_{Slab\_1} - n_{wg}\right)L_{Slab\_1} + n_{sl}L_{sl}\right)\right] \qquad (5)$$

$$= \cos\left[\phi_{slab-wg} + \phi_{sl}\right]$$

The mode indices n_{wg}, n_{slab_1}, n_{sl} have different frequency dispersion. We kept the phase (ϕ_{slab_wg}), arising from $\frac{2\pi}{\lambda}\left(n_{slab\_1} - n_{wg}\right)L_{slab\_1}$, constant between different devices in each set of measurements by simply ensuring that the physical lengths and widths of the slabs are the same for each nanofabricated device. The remaining phase variation therefore is generated only by the photonic crystal superlattice ($\phi_{sl} = \frac{2\pi}{\lambda}n_{sl}L_{sl}$). If n_{sl} is equal to zero, ϕ_{sl} is zero too, hence the total phase difference ϕ in the interferometer arises only from the ϕ_{slab_wg} component and is the same for all the devices in each set. Therefore, the sinusoidal oscillations in the transmission and the free spectral range are determined only by ϕ_{slab_wg}.

5.2 Experimental results for zero phase

Figure 11a shows the interference pattern for d_2/d_1=0.78 with 7 unit cells in the PhC layer. As can be seen in this figure, outside the zero-$\bar{n}$ spectral region the fringes differ from each other both in wavelength and the FSR, but overlap almost perfectly within the zero-$\bar{n}$ spectral domain.

To illustrate the phase evolution, we show in Figure 12a the FSR values for each of the devices examined – specifically we calculate the spectral spacing between the transmission minima and plot its dependence on the center wavelength between the two neighboring minima. As these measurements illustrate, in the zero-$\bar{n}$ spectral domain the FSR corresponding to each of the devices approaches the same value, indicating that the corresponding phase difference is zero or, alternatively, that the optical path remains unchanged. This is a surprising conclusion since the physical path is certainly not the same in all the cases. This apparent paradox has a simple explanation: although the physical path varies among the three cases the optical path is the same (and equal to zero) as the spatially averaged refractive index of the three superlattices vanishes. In other words, within the zero-$\bar{n}$ spectral region the photonic superlattice emulates the properties of a zero phase delay line. The output corresponding to the structures with d_2/d_1=0.8 and 7 unit cells in the PhC layer is shown in Figure 11b whereas the FSR values are plotted in Figure 12b. Finally, Figure 11c and Figure 12c show the interference patterns for the case of d_2/d_1=0.8 and 9 unit cells in the PhC layer. Again, both the FSR (Figure 12b-c) and the absolute wavelength values (Figure 11b-c) overlap, proving the zero phase variation across the superlattice.

It should be noted that in all our plots of experimental data we have used the raw data and as such there is no data post-processing, except for the intensity rescaling. Measurements are taken 3 times with 500 pm resolution for Figure 3d and Figure 11a-e; 100 pm and 500 pm

resolutions for Figure11a and 200 pm and 500 pm resolutions for Figure 11b-c. There is ~ 1% deviation between Figure 11e and Figure 11b-c in terms of the center frequency of the zero-$\bar{n}$ region. This is so because of the fabrication differences between the samples. For Figure 11b-c, the r/a ratio was ~5% smaller (~0.264) resulting in the shift of the band structure to lower frequencies, and, consequently to a shift of the zero-$\bar{n}$ bandgap. We verified the location of the zero-$\bar{n}$ bandgap (~1565 nm) by performing the transmission measurements described before. Thus, the spectral location of the zero-$\bar{n}$ bandgap can be tracked from the phase measurements, as the spectral region of small amplitude oscillations in the transmission spectra correspond to the zero-$\bar{n}$ bandgaps.
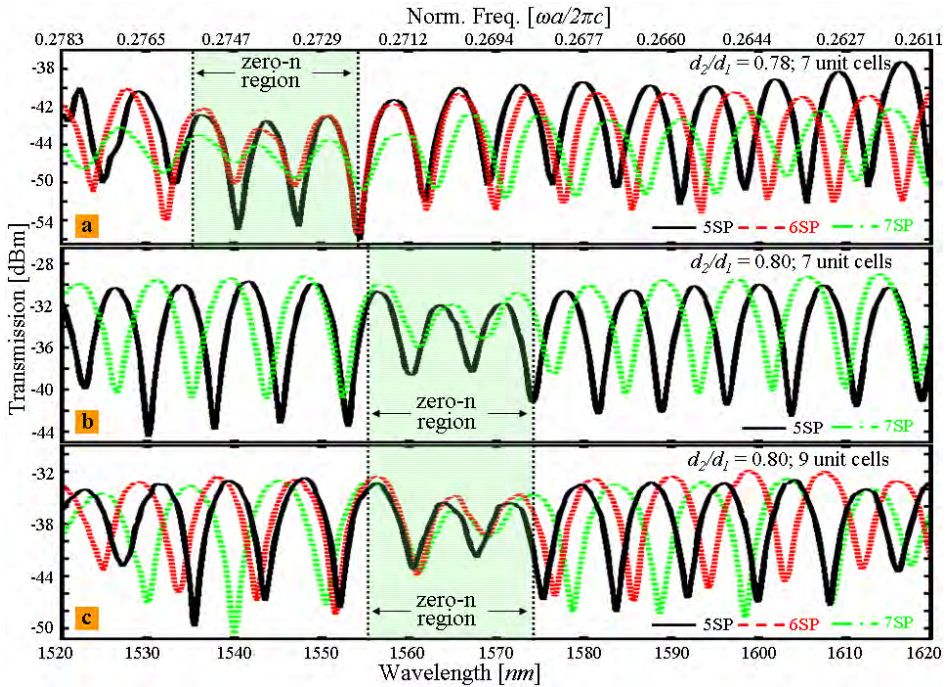

Fig. 11. **Phase measurements. a,** Output of the MZI with increasing number of superperiods (5, 6, and 7 SP) on one arm and with length-adjusted single mode channel waveguides on the other arm. Each PhC layer contains 7 unit cells (d_1=2.564 µm) and d_2/d_1 =0.78. **b,** Same as in **a**, but for d_2/d_1 =0.8. **c,** Same as in b, with each PhC layer containing 9 unit cells (d_1=3.297 µm).

In summary, we have demonstrated for the first time zero-phase delay in negative-positive index superlattices, in addition to the simultaneous observations of deterministic zero-$\bar{n}$ gaps that can remain invariant to geometric changes and band-to-band transitions in negative-positive index photonic crystal superlattices. Through the interferometric measurements, the transmissive binary superlattices with varying lengths are shown unequivocally to enable the absolute control of the optical phase. The engineered control of the phase delay in these near-zero superlattices can be implemented in chip-scale

transmission lines with deterministic phase array control, even with technological potential in phase-insensitive image processing, phase-invariant field for electromagnetic cloaking, and the arbitrary radiation wavefront reshaping of antennae from first principles.
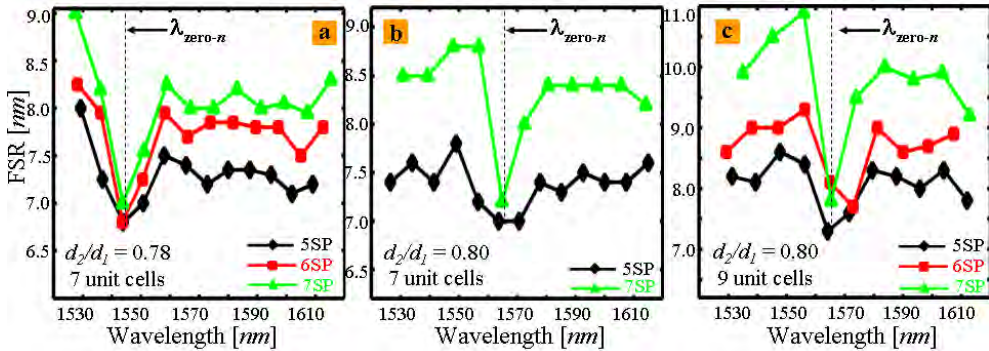

Fig. 12. **Free spectral range wavelength dependence corresponding to superlattices in Figure 4. a-c,** Free spectral range extracted from the data in Figure 4a-c. At the zero-$\bar{n}$ bandgap wavelength, the free spectral range converges to the same value, which proves the zero phase contribution from the added superperiods.

6. References

[1] Veselago, V. G. The electrodynamics of substances with simultaneously negative values of ε and μ. *Usp.Fiz.Nauk* 92, 517 (1964) [*Sov.Phys.Usp.* 10, 509 (1968)].

[2] Pendry, J. B. Time Reversal and Negative Refraction. *Science* 322, 71 (2008).

[3] Shelby, R. A., Smith, D. R. & Schultz, S. Experimental verification of a negative index of refraction. *Science* 292, 77 (2001).

[4] Valentine, J. et al. Three-dimensional optical metamaterial with a negative refractive index. *Nature* 455, 376 (2008).

[5] Li, N. et al. Three-dimensional photonic metamaterials at optical frequencies. *Nature Mat.* 7, 31 (2008).

[6] Gramotnev, D. K. & Bozhevolnyi, S. I. Plasmonics beyond the diffraction limit. *Nature Phot.* 4, 83 (2010).

[7] Shalaev, V. M. Optical negative-index metamaterials. *Nature Photonics* 1, 41 (2007).

[8] Kundtz, N. & Smith, D. R. Extreme-angle broadband metamaterial lens. *Nature Mat.* 9, 129 (2010).

[9] Panoiu, N. C. & Osgood, R. M. Influence of the dispersive properties of metals on the transmission characteristics of left-handed materials. *Phys. Rev. E* 68, 016611 (2003).

[10] Zhang, S. et al. Demonstration of near-infrared negative-index metamaterials. *Phys. Rev. Lett.* 95, 137404 (2005).

[11] Liu, R. et al. Experimental Demonstration of Electromagnetic Tunneling Through an Epsilon-Near-Zero Metamaterial at Microwave Frequencies. *Phys. Rev. Lett.* 100, 023903 (2008).

[12] Tsakmakidis, K. L., Boardman, A. D. & Hess, O. 'Trapped rainbow' storage of light in metamaterials. *Nature* 450, 397 (2007).

[13] Yao, J. et al. Optical Negative Refraction in Bulk Metamaterials of Nanowires. *Science* 321, 930 (2008).

[14] Xi, S. et al. Experimental Verification of Reversed Cherenkov Radiation in Left-Handed Metamaterial. *Phys. Rev. Lett.* 103, 194801 (2009)

[15] Hoffman, A. J. et al. Negative refraction in semiconductor metamaterials. *Nature Mat.* 6, 946 (2007).

[16] Grigorenko, A. N. et al. Nanofabricated media with negative permeability at visible frequencies. *Nature* 438, 335 (2005).

[17] Dolling, G., Enkrich, C., Wegener, M., Soukoulis, C. M. & Linden, S. Simultaneous Negative Phase and Group Velocity of Light in a Metamaterials. *Science* 312, 892 (2006).

[18] Pollard, R. J. et al. Optical Nonlocalities and Additional Waves in Epsilon-Near-Zero Metamaterials. *Phys. Rev. Lett.* 102, 127405 (2009).

[19] Jin, Y., Zhang, P. & He, S. Squeezing electromagnetic energy with a dielectric split ring inside a permeability-near-zero metamaterial. *Phys. Rev. B* 81, 085117 (2010)

[20] Hsueh, W. J., Chen, C. T. & Chen, C. H. Omnidirectional band gap in Fibonacci photonic crystals with metamaterials using a band-edge formalism. *Phys. Rev. A* 78, 013836 (2008).

[21] Xu, J.-P., Yang, Y.-P., Chen, H. & Zhu, S.-Y. Spontaneous decay process of a two-level atom embedded in a one-dimensional structure containing left-handed material. *Phys. Rev. A* 76, 063813 (2007).

[22] Chatterjee, R. et al. Achieving subdiffraction imaging through bound surface states in negative-refraction photonic crystals in the near-infrared range. *Phys. Rev. Lett.* 100, 187401 (2008).

[23] Decoopman, T., Tayeb, G., Enoch, S., Maystre, D. & Gralak, B. Photonic Crystal Lens: From Negative Refraction and Negative Index to Negative Permittivity and Permeability. *Phys. Rev. Lett.* 97, 073905 (2006).

[24] Lu, Z. et al. Three-Dimensional Subwavelength Imaging by a Photonic-Crystal Flat Lens Using Negative Refraction at Microwave Frequencies. *Phys. Rev. Lett.* 95, 153901 (2005).

[25] Parimi, P. V., Lu, W. T., Vodo, P. & Sridhar, S. Photonic crystals: Imaging by flat lens using negative refraction. *Nature* 426, 404 (2003).

[26] Notomi, M. Theory of light propagation in strongly modulated photonic crystals: Refractionlike behavior in the vicinity of the photonic band gap. *Phys. Rev. B* 62, 10696 (2000).

[27] Li, J., Zhou, L., Chan, C. T. & Sheng, P. Photonic Band Gap from a Stack of Positive and Negative Index Materials. *Phys. Rev. Lett.* 90, 083901 (2003).

[28] Panoiu, N. C., Osgood, R. M., Zhang, S. & Brueck, S. R. J. Zero-n bandgap in photonic crystal superlattices. *J. Opt. Soc. Am. B* 23, 506 (2006).

[29] Kocaman, S. et al. Observations of zero-order bandgaps in negative-index photonic crystal superlattices at the near-infrared. *Phys. Rev. Lett.* 102, 203905 (2009).

[30] Kocaman, S et al. Zero phase delay in negative-index photonic crystal superlattices, *Nature Photonics* 5, 499 (2011).

[31] Yuan, Y. et al. Experimental verification of zero order bandgap in a layered stack of left-handed and right-handed materials. *Opt. Express* 14, 2220 (2006).

[32] Zhang, L., Zhang, Y., He, L., Li, H. & Chen, H. Experimental investigation on zero-n_{eff} gaps of photonic crystals containing single-negative materials. *Eur. Phys. J. B.* 62, 1 (2008).

[33] Hegde, R. S. & Winful, H. G. Zero-n gap soliton. *Opt. Lett.* 30, 1852 (2005).

[34] Mocella, V. et al. Self-Collimation of Light over Millimeter-Scale Distance in a Quasi-Zero-Average-Index Metamaterial. *Phys. Rev. Lett.* 102, 133902 (2009).

[35] Enoch, S., Tayeb, G., Sabouroux, P., Guérin, N. & Vincent, P. A Metamaterial for Directive Emission. *Phys. Rev. Lett.* 89, 213902 (2002).

[36] Ziolkowski, R. W. Propagation in and scattering from a matched metamaterial having a zero index of refraction. *Phys. Rev. E* 70, 046608 (2004).

[37] Litchinitser, N. M., Maimistov, A. I., Gabitov, I. R., Sagdeev, R. Z. & Shalaev, V. M. Metamaterials: electromagnetic enhancement at zero-index transition. *Opt. Lett.* 33, 2350 (2008).

[38] Wang, L.-G., Li, G.-X. & Zhu, S.-Y. Thermal emission from layered structures containing a negative-zero-positive index metamaterial. *Phys. Rev. B* 81, 073105 (2010).

[39] Shadrivov, I. V., Sukhorukov, A. A. & Kivshar, Y. S. Complete band gaps in one-dimensional left-handed periodic structures. *Phys. Rev. Lett* 95, 193903 (2005).

[40] Hao, J., Yan, W. & Qiu, M. Super-reflection and cloaking based on zero index metamaterial. *Appl. Phys. Lett.* 96, 101109 (2010).

[41] Jiang, H., Chen, H., Li, H., Zhang, Y. & Zhu, S. Omnidirectional gap and defect mode of one-dimensional photonic crystals containing negative-index materials. *Appl. Phys. Lett.* 83, 5386 (2003).

[42] Bria, D. et al. Band structure and omnidirectional photonic band gap in lamellar structures with left-handed materials. *Phys. Rev. E* 69, 066613 (2004).

[43] A.R. Davoyan, I. V. Shadrivov, A.A. Sukhorukov, and Y.S. Kivshar, Bloch oscillations in chirped layered structures with metamaterials. *Opt. Express* 16, 3299 (2008).

[44] M.D. Henry, C. Welch, and A. Scherer. Techniques of cryogenic reactive ion etching in silicon for fabrication of sensors. *J. Vac. Sci. Technol.* A 27, 1211 (2009).

[45] Rsoft Design Group Inc, FullWAVE™, Ossining, NY.

[46] X. Wang *et. al.*, "Effects of disorder on subwavelength lensing in two-dimensional photonic crystal slabs", Phys. Rev. B 71, 085101 (2005).

[47] Vlasov, Y.A., O'Boyle, M., Hamann, H.F., and McNab, S.J. Active control of slow light on a chip with photonic crystal waveguides, *Nature* 438, 65 (2005).